

Supplementary Information for

***In-Situ* Observation of Initial Stage in Dielectric Growth, and Deposition of Ultrahigh Nucleation Density Dielectric on Two-Dimensional Surfaces.**

Jun Hong Park[†], *Hema C.P. Movva*[§], *Evgeniy Chagarov*[‡], *Kasra Sardashti*[†], *Harry Chou*[§], *Iljo Kwak*[†], *Kai-Ting Hu*^{||}, *Susan K. Fullerton-Shirey*[⊥], *Pabitra Choudhury*[#], *Sanjay K. Banerjee*[§],
Andrew C. Kummel[†], *‡**

[†]Materials Science & Engineering Program, [‡]Departments of Chemistry & Biochemistry,

^{||}Mechanical and Aerospace Engineering, University of California, San Diego.

[§]Electrical and Computer Engineering, University of Texas at Austin.

[⊥]Department of Electrical Engineering, University of Notre Dame.

[#]Department of Chemical Engineering, New Mexico Tech.

*E-mail: akummel@ucsd.edu.

Materials and Methods

1. In-Situ ALD and STM system.
2. Deposition of TiOPc monolayer on HOPG by dip coating
3. TiOPc molecular structure.
4. STS calibration on HOPG and measurement of electronic surface bandgap by $(dI/dV)/(I/V)$.
5. CVD growth of single layer graphene and transfer onto SiO₂/Si.
6. DFT Calculations.
7. Fabrication of metal-dielectric-TiOPc-graphene capacitors and dual-gated graphene FETs.

Supplementary data

1. TiOPc monolayer on MoS₂.
2. Charge density plot near Dirac point of TiOPc/graphene.
3. Binding energy of DMA and TMA with TiOPc calculated by DFT.
4. Sequential DMA binding on single TiOPc molecule.
5. Inducing amorphous surface on TiOPc/HOPG, after forming of TMA chemisorbates.
6. AFM images after ALD on bare HOPG, TiOPc/HOPG and TiOPC/graphene.
7. Observation charge trap states in AlO_x/TiOPc/HOPG by STS.
8. Capacitance-Voltage curves with expanded frequencies.
9. MoS₂-ALD dielectric-TiOPc-graphene interlayer device.

Materials and Methods

1. In-situ ALD and STM system.

The entire system consists of five sets of chambers, shown in Fig. 1: the STM chamber, the preparation chamber, the load lock chamber, the atomic layer deposition (ALD) chamber, and the organic MBE chamber. Each chamber is pumped by ion or turbo pumps and separated by gate valves. The main (sample preparation) and STM chambers are pumped by ion pumps; the base pressure of each is below 1×10^{-10} and 2×10^{-11} torr, respectively. The organic MBE, ALD, and load-lock chambers are pumped by turbo molecular pumps (TMP); the base pressures of the organic MBE, load lock, and ALD chambers are 5×10^{-9} , 1×10^{-7} and 3×10^{-6} torr, respectively. After deposition of a TiOPc seed layer on HOPG or on single-layer graphene, the samples are transferred to the ALD chamber through the load-lock chamber. After the samples are exposed to ALD, the samples are transferred back to main chamber and subsequently transferred to the STM stage. The samples are never exposed to ambient conditions during this entire process.

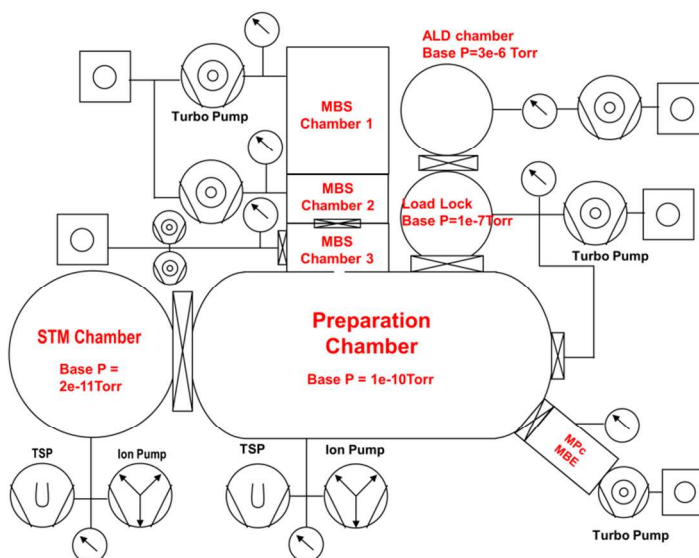


Figure S1. Schematic diagram of STM and ALD chambers with in-situ probes. The base pressure of main chamber is 1×10^{-10} torr, while the base pressure of STM chamber is 2×10^{-11} torr.

2. Deposition of TiOPc monolayer on HOPG by dip coating.

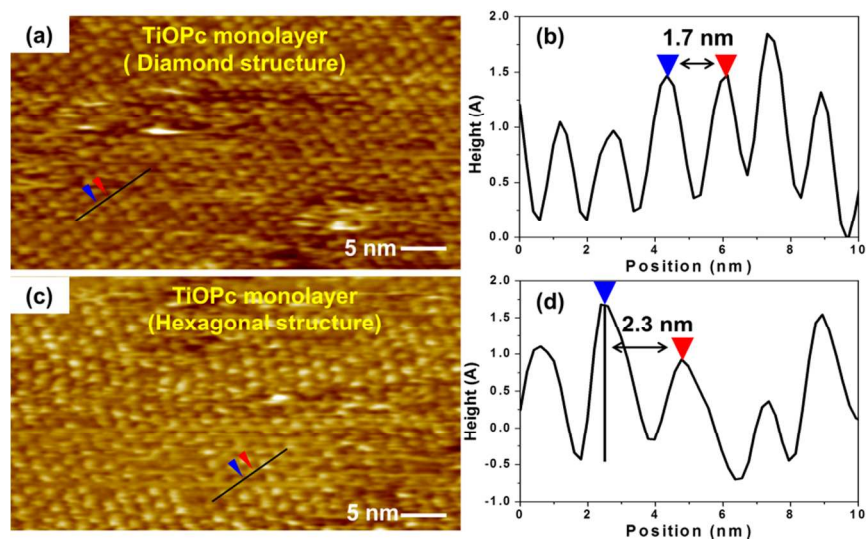


Figure S2. TiOPc monolayer deposited by dip coating. STM images were taken on two different areas on the same sample ($V_s = 2\text{ V}$, $I_t = 40\text{ pA}$). (a) Empty state STM images in area with square structure; (b) Line trace corresponding to Fig. S3(a), (c) Empty state STM in area with hexagonal structure; (d) Line trace corresponding to Fig. S3(c). The data is consistent with the formation of a TiOPc monolayer with two different symmetries.

In addition to the MBE technique described in the manuscript, TiOPc monolayers can also be deposited by solution deposition. A $5\text{ }\mu\text{M}$ TiOPc solution was prepared by dissolving TiOPc in toluene (Fisher Scientific). The HOPG or graphene samples were immerse in the TiOPc/toluene solution for 30 min in air. Afterwards, the samples were dried in air until the solvent was completely evaporated. It is noted that the coverage of the TiOPc layer can be controlled by the solution concentration^{1,2}. Dried, thick TiOPc samples were transferred into the preparation vacuum chamber *via* the load-lock chamber as shown in Fig S1. After the sample was annealed at 523 K for 6 min, a monolayer of TiOPc was obtained. As shown in Fig S3, although a TiOPc monolayer is deposited on HOPG, two different molecular lattice structures are observed on the same sample. Some of areas show square symmetry in Fig. S3 (a) and (b),

similar to MBE-deposited TiOPc monolayers, while the other areas show hexagonal crystal structure, as shown in Fig S3 (c) and (d). The different crystal structures give rise to differences in spacing (1.7 vs 2.3 nm) as shown in Fig. S3 (b) and (d).

3. TiOPc molecular structure.

TiOPc is a polar metal organic complex; the Ti atom is located at the center while carbon atoms form the basic backbone of the molecule as shown in Fig. S2. N atoms are located at central inner area surrounding the metal center. At the perimeter of the TiOPc, the carbons form aromatic rings terminated by H atoms. The polarity of the TiOPc molecule arises from the O atom bonded to the central Ti atom.

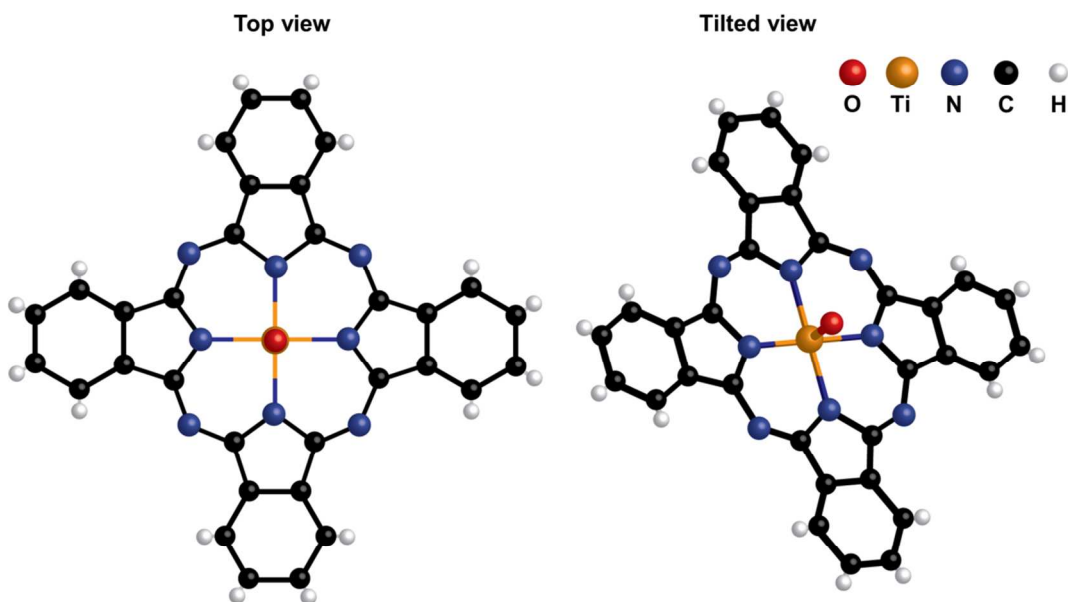


Figure S3. Schematic model for the molecular structure of TiOPc. The Ti atom is located at the center of the TiOPc molecule, and the O atom is bonded to the central Ti.

4. STS calibration on HOPG and measurement of electronic surface bandgap by $(dI/dV)/(I/V)$.

A. STS calibration on HOPG.

To avoid inducing artifacts in the STM images and STS, W Tips were calibrated on clean, HOPG surfaces before STM experiments on TiOPc and $\text{AlO}_x/\text{TiOPc}$ surfaces. In figure S4, a zero band gap and linear dispersion of DOS are observed on HOPG, consistent with previous reports^{3, 4}.

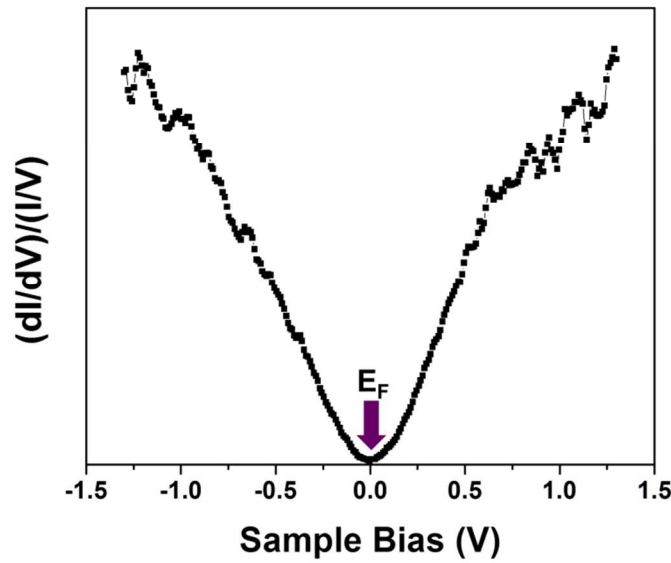


Figure S4. $(dI/dV)/(I/V)$ spectrum of HOPG surface for tip calibration. A linear dispersion of DOS and zero band gap are shown, as expected for an HOPG surface.

B. Measuring the electronic surface band gap by $(dI/dV)/(I/V)$.

After the STS data were recorded, the differential conductance (dI/dV) was normalized by (I/V) . The band gap measurement is based on the Feenstra method.^{5, 6} The first step in defining the band gap is to determine the valance (VB) and conduction band (CB) onset bias, consistent with VB maxima and CB minima respectively. As shown in Fig. S7, straight lines are drawn through $(dI/dV)/(I/V)$. The VB

maxima and CB minima are given by the intersection of the lines: VB onset (VB maxima) = -1.62 V; CB onset (CB minima) = +1.74 V. Therefore, the surface band gap of $\text{AlO}_x/\text{TiOPc}/\text{HOPG}$ after a 1 cycle of ALD is 3.36 eV.

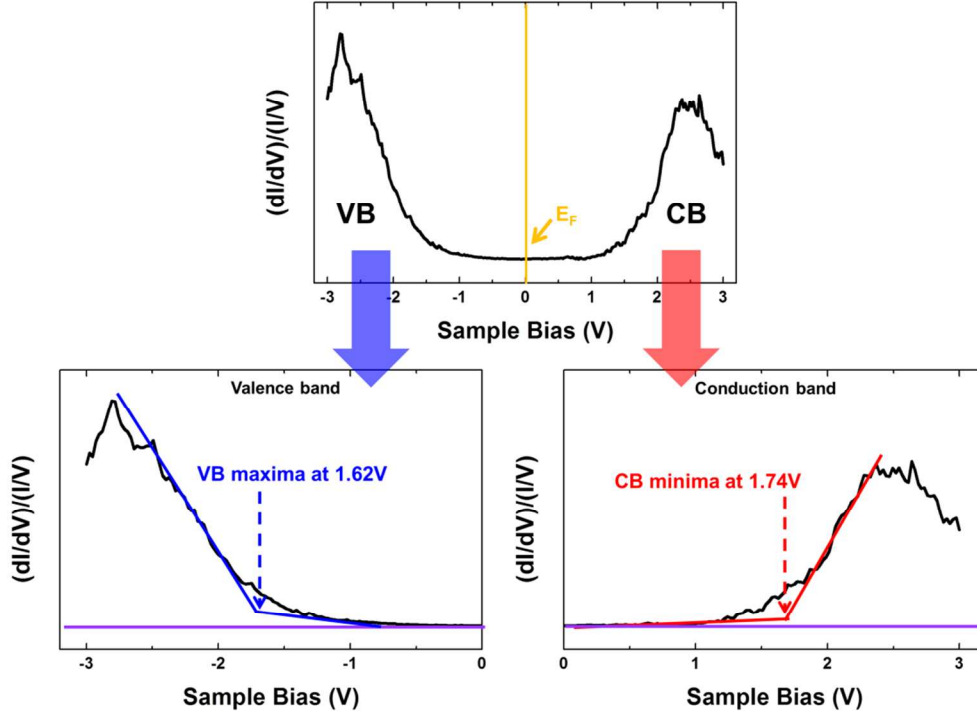


Figure S5. Example of STS bandgap measurement by determining the onset positions. STS data were taken on a sample of $\text{AlO}_x/\text{TiOPc}/\text{HOPG}$ with 1 cycle of ALD. The valance band (VB) maxima is located at -1.62 V, while conduction band (CB) minima is positioned at +1.74V, consistent with 3.36 eV band gap.

5. CVD growth of single layer graphene and transfer onto SiO_2/Si .

Single layer graphene was grown on Cu foil in a hot wall furnace at 1237 K using methane gas as a precursor⁷. To transfer the graphene onto the SiO_2/Si substrates, poly-methyl methacrylate (PMMA) was spin-coated onto the graphene/Cu foil. The PMMA/graphene/Cu foil was placed in an aqueous solution of ammonium persulfate (0.1 M, Sigma Aldrich) to etch the copper. The floating

PMMA/graphene film was rinsed several times in distilled water to remove etchant residue and then transferred to a clean DI water bath. The target SiO₂/Si substrate was placed in the water bath and used to “scoop-out” the PMMA/graphene film⁸. The substrate with PMMA/graphene was allowed to dry in a vacuum desiccator for several hours, and subsequently heated to 453 K on a hot plate for 30 min in air to flatten out the graphene and minimize wrinkles. The PMMA was removed in an acetone bath. A final anneal was performed at 623 K for 8 hours in a high vacuum chamber (base pressure $\sim 1 \times 10^{-6}$ Torr) to minimize PMMA residue.

6. DFT Calculations.

Density functional theory (DFT) calculations were performed using the Vienna *ab-initio* Simulation Package (VASP) using the projector augmented-wave (PAW) pseudopotentials with plane-wave energy cutoff of 400 eV⁹⁻¹⁴. All DFT calculations were spin-polarized. The Perdew–Burke–Ernzerhof (PBE-GGA) exchange-correlation functional was applied^{15, 16}. An efficient semiempirical scheme proposed by Grimme to account for van der Waals interactions was employed for all calculations^{17, 18}. The graphene surface is periodic in the x and y directions. In z dimension, a vacuum layer of ~ 20 Å was added to avoid spurious interaction through periodic boundary conditions. Ionic relaxation was performed using conjugate-gradient relaxation method with force tolerance level below 0.01 eV/Å. A $5 \times 5 \times 1$ Gamma-centered, k-point grid was used for sampling in reciprocal space. The electronic energies converged below 10^{-6} eV. A Gaussian smearing width of 0.01 eV was applied.

The binding energy of the dimethyl aluminum (DMA) adsorbate to the TiOPc/graphene (TiOPc-G) layer was calculated as follows:

$$E_{bind} = E_{tot}(DMA + TiOPc-G) - E_{tot}(TiOPc-G) - E_{tot}(DMA)$$

where E_{bind} is the binding energy of DMA to the TiOPc functionalized graphene surface, $E_{tot}(DMA)$ is the total energy of DMA in the gas phase, $E_{tot}(TiOPc-G)$ is the total energy of the TiOPc

functionalized surface without the DMA adsorbate, and $E_{tot}(DMA + TiOPc-G)$ is the total energy of the TiOPc functionalized graphene surface with DMA absorbed ($A 3 \times 3 \times 1$ Monkhorst-Pack k-point). Note that negative value of E_{bind} corresponds to binding (attraction) and positive value to repulsion.

7. Fabrication of metal-dielectric-TiOPc-graphene capacitors and dual gated graphene FETs.

A. Fabrication of metal-dielectric-TiOPc-graphene capacitors.

Before deposition of TiOPc onto graphene, an Au bottom contact (thickness: 50 nm, contact size: 2 mm X 2mm) was deposited using e-beam evaporation onto graphene/SiO₂/Si as shown in Fig S6(a). Graphene/SiO₂/Si samples were transferred to a UHV chamber; afterwards TiOPc seed layers were deposited on graphene/SiO₂/Si *via* MBE. The TiOPc/graphene/SiO₂/Si samples were transferred immediately in air from the UHV chamber to a commercial ALD reactor (Beneq) for dielectric deposition (50 cycles of ALD). Next, Ni electrodes (50 nm) were thermally evaporated onto AlO_x/TiOPc/graphene/SiO₂/Si, through a shadow mask, forming an array of 200 µm diameter circular electrodes. The size of electrodes was verified by optical microscopy, as shown in Fig S6(b). Capacitance-voltage and resistance-voltage were measured under ambient conditions with a probe station (Agilent B1500A Semiconductor Analyzer). During electrical measurements, metal electrodes were contacted by W needle probes to avoid damage to the thin dielectrics, while SiO₂/Si substrates were grounded.

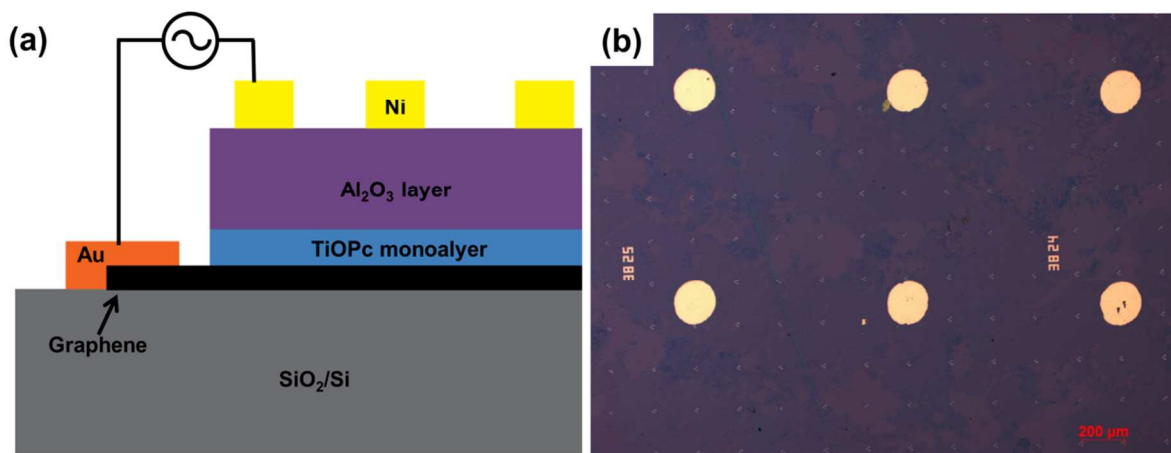


Figure S6. Cross-sectional schematic of graphene capacitor and optical image of surface. (a) Schematic metal-TiOPc-graphene-SiO₂-Si capacitor. (b) Optical micrograph of Ni gates deposited on AlO_x/TiOPc/graphene/SiO₂/Si.

B. Fabrication of dual-gated graphene field effect transistors.

Graphene FETs were fabricated using the Scotch tape method by mechanical exfoliation from natural graphite (Structure Probe, Inc) onto thermally grown 300 nm SiO₂ on *n*-type Si substrates. Raman spectroscopy and optical microscopy were employed to identify the number of graphene layers. The source and drain regions (source/drain separation: 3.3 μm) were defined on single layer graphene by electron beam lithography (EBL); afterwards Ni source/drain contacts were deposited onto graphene using an e-beam evaporation. The fabricated graphene FETs were annealed at 623 K for 8 h in vacuum ($\sim 1 \times 10^{-6}$ Torr) to remove resist residue from device fabrication. Similar to the graphene capacitors, fabricated devices were transferred into the UHV chamber for deposition of a TiOPC seed layer on graphene; afterwards a dielectric layer with 40 cycles was deposited in the ALD reactor. Subsequently, the top-gate region was defined on the AlO_x/TiOPc/graphene/SiO₂ using EBL, followed by e-beam evaporation of 50 nm Ni top-gate contacts. All electrical measurements were performed using a probe station and W tips in ambient condition (Cascade Summit 11000B).

Supplementary data

1. TiOPc monolayer on bulk MoS₂.

In addition to graphene, the flat-lying TiOPc monolayer can also be obtained on other transition metal dichalcogenide (TMD) surfaces. The bulk MoS₂ samples were purchased from SPi supplier (Structure Probe, Inc) and cleansed by multiple mechanical exfoliated. The cleaned bulk MoS₂ samples were transferred into UHV chamber (1×10^{-10} torr), then annealed at 750 K for 3 h to remove contaminants introduced from ambient air. As shown in Fig S7(a), after TiOPc deposition by MBE, a periodic array of TiOPc molecules is observed on a bulk MoS₂ surface. Similar to TiOPc/HOPG, the square lattice structure is formed. These results show that the TiOPc seed layer for ALD can be extended to other 2D materials.

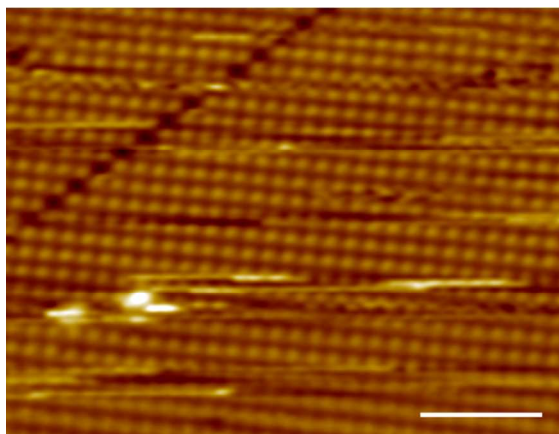


Figure S7. TiOPc monolayer deposited on MoS₂. Empty state STM image showing a TiOPc monolayer forming a square lattice on bulk MoS₂. Scale bar indicates 10 nm. ($V_s = 2$ V, $I_t = 20$ pA)

2. Charge density plot near Dirac point of TiOPc/graphene.

For the TiOPc/Graphene system, the band-decomposed charge density within ± 0.25 eV of the Fermi level is visualized in Fig S8. All the states near the Dirac point on the graphene are consistent with

TiOPc molecules not perturbing the band structure of graphene near the Dirac point. This calculation was performed with the Perdew–Burke–Ernzerhof (PBE-GGA) exchange-correlation functional and 3x3x1 k-point Gamma center sampling.

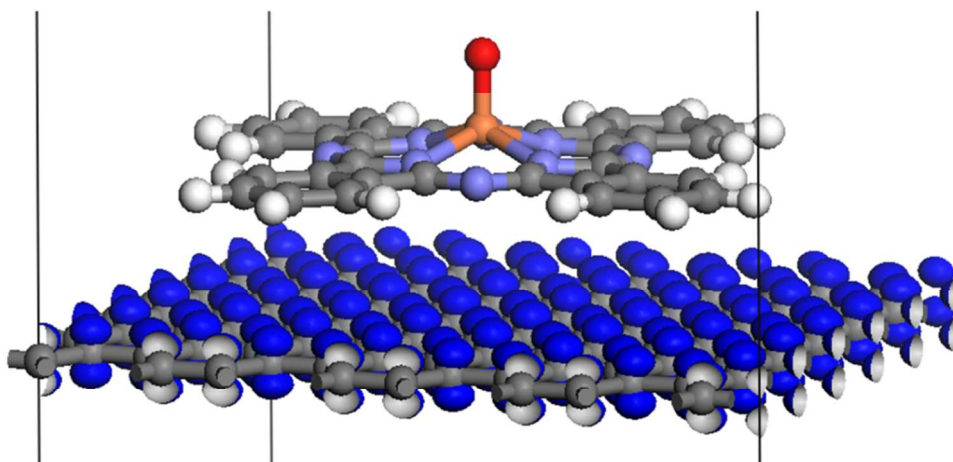


Figure S8. Band decomposed charge density near the Dirac point of graphene in TiOPc/graphene.

The charge density within +/- 0.25 eV of the Fermi level of TiOPc/graphene is visualized as blue. 3x3x1 k-point Gamma center was sampled during calculation.

3. Binding energy of DMA and TMA with TiOPc calculated by DFT.

A. Density functional theory (DFT) models of DMA/TiOPc/HOPG

To understand the mechanism that provides the high nucleation density of AlO_x on the TiOPc seed layer, DFT was used to calculate the binding energies of the ALD precursor on three available binding sites on TiOPc: O, N and C, as shown in Fig. S9. It is assumed that TMA dissociates into DMA and that the coverage of DMA is limited by the number of thermally stable binding sites at the 373 K reaction temperature. The central O has the strongest binding energy with DMA (3.08 eV), the N sites

have an intermediate binding energy (2.02 eV), and the C sites have the lowest binding energy (1.53 eV). Although O, N and C have different binding energies with DMA, all sites can hold DMA at 373 K to form the oxide during ALD.

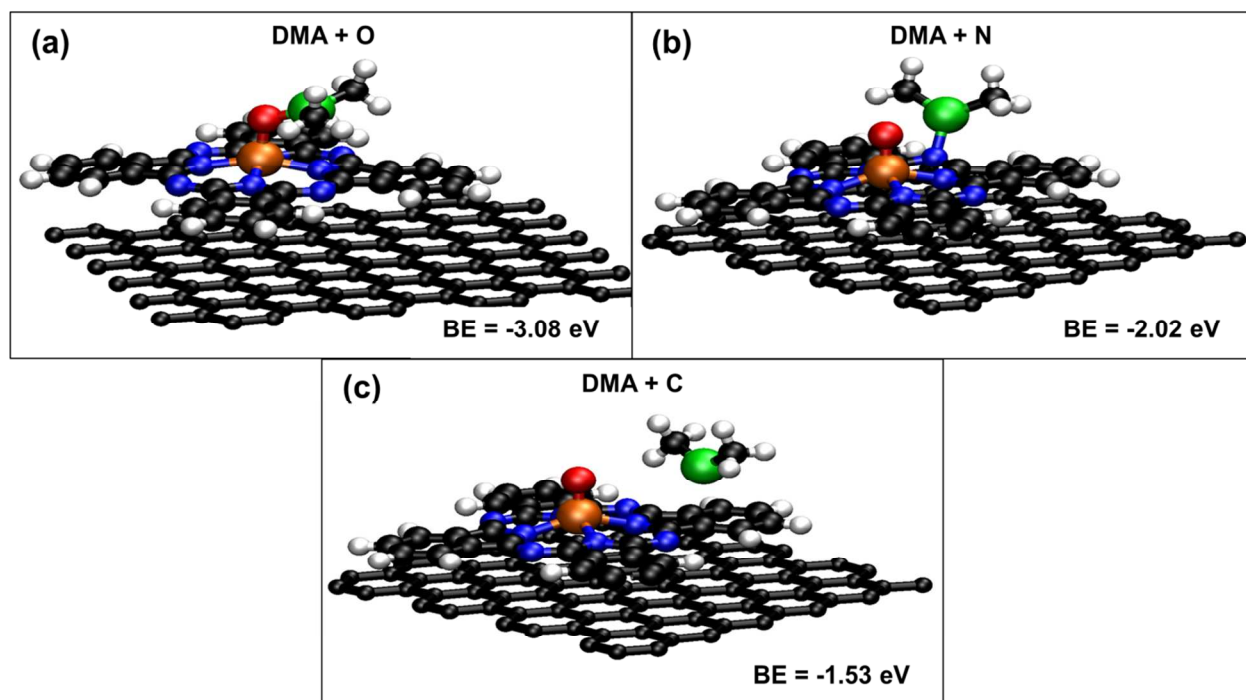


Figure S9. Density functional theory (DFT) calculation for DMA binding with TiOPc on graphene. DMA bonds with (a) O (b) N and (c) C of TiOPc. The binding energy was calculated with most stable binding configuration.

B. Density functional theory (DFT) models of TMA/TiOPc/HOPG.

Trimethyl aluminum (TMA) dissociates into dimethyl aluminum (DMA) at even at 300K^{19, 20}. However, If TMA does not dissociate, undissociated TMA has a much lower binding energy than DMA with O and N for molecular chemisorption. In Fig. S9, DFT calculations show that TMA molecularly chemisorbs to the O site with 1.1eV binding energy and to N with 0.72eV consistent with the instability of TMA binding sites at 373K. However, since it is favorable for TMA dissociates into DMA at 373K, it

can be assumed most of the TMA dissociatively chemisorbs on the TiOPc seed layer, rather than undissociated TMA binding with TiOPc molecules^{19, 20}.

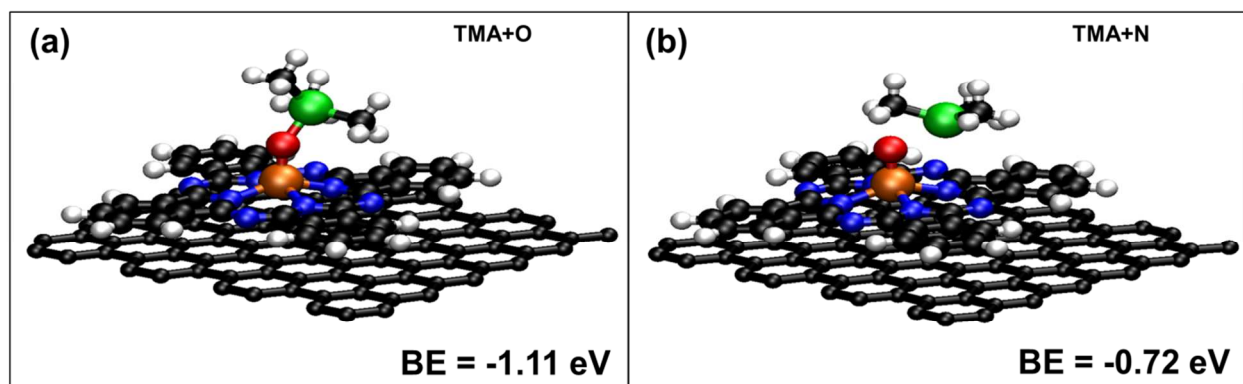


Figure S10. Density functional theory (DFT) calculation for TMA binding with TiOPc on graphene TMA bonds with (a) O and (b) N. The binding energy was calculated with most stable binding configuration.

4. Sequential DMA binding on single TiOPc molecule.

DMA can react with multiple sites on a single TiOPc molecule simultaneously. Binding energies of DMA with TiOPc were calculated for multiple DMA reacting sequentially with TiOPc, as shown in Fig S10. After initial DMA binding with the O of TiOPc (3.08 eV), a second DMA molecule reacts with the N of TiOPc with 2.33 eV binding energy, and a third DMA molecule has the same binding energy (2.33 eV). Binding between TiOPc and a fourth DMA molecule has a slightly smaller energy (2.21 eV), while the fifth molecule is 2.21 eV. DFT calculations show that for 5 DMA molecules reacting with TiOPc, all binding energies are greater than 2 eV, consistent with high nucleation density AlO_x in STM images. The high binding energies indicates that the reaction of multiple DMA with single TiOPc molecule can occur simultaneously or sequentially, resulting in a high nucleation density during ALD, even at 393 K.

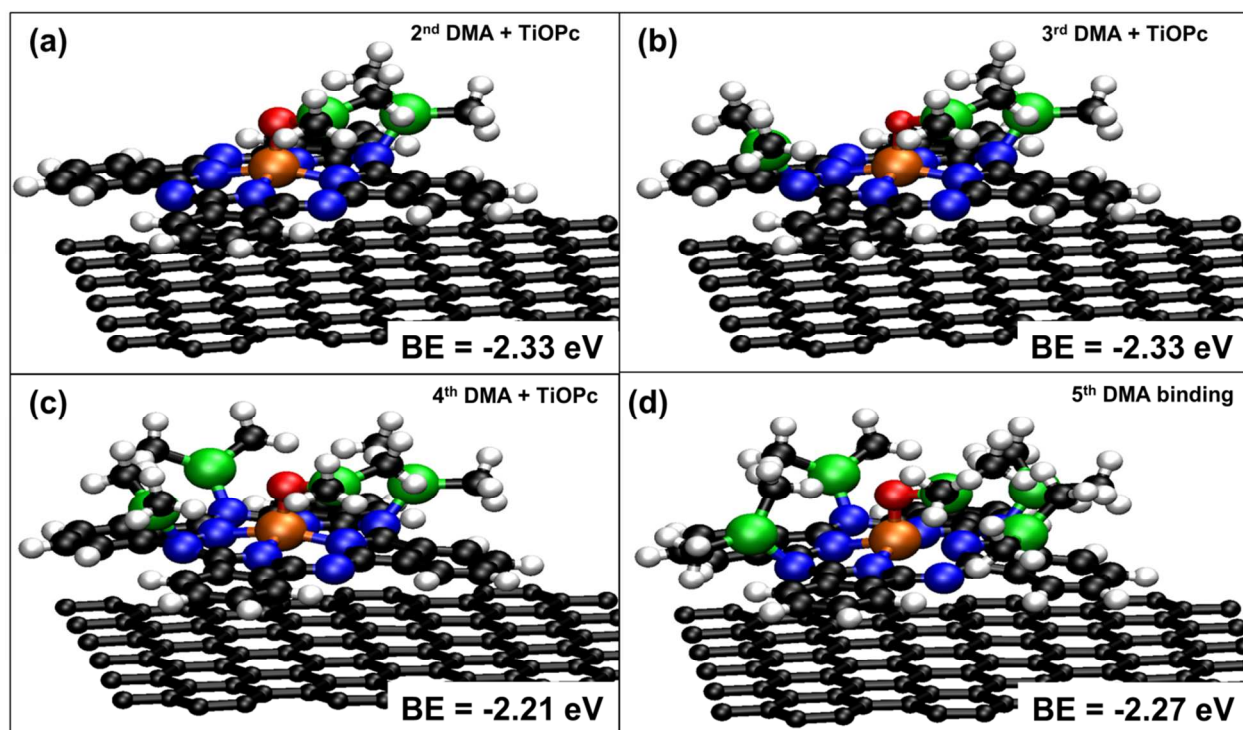


Figure S11. Density functional theory (DFT) model for sequential DMA binding on single TiOPc molecule. (a) Second DMA binding with TiOPc *via* N, (b) Third DMA binding with TiOPc *via* N, (c) Fourth DMA binding with TiOPc *via* N. (d) fifth DMA binding with TiOPc *via* N.

5. Inducing amorphous surface on TiOPc/HOPG, after forming of TMA chemisorbates.

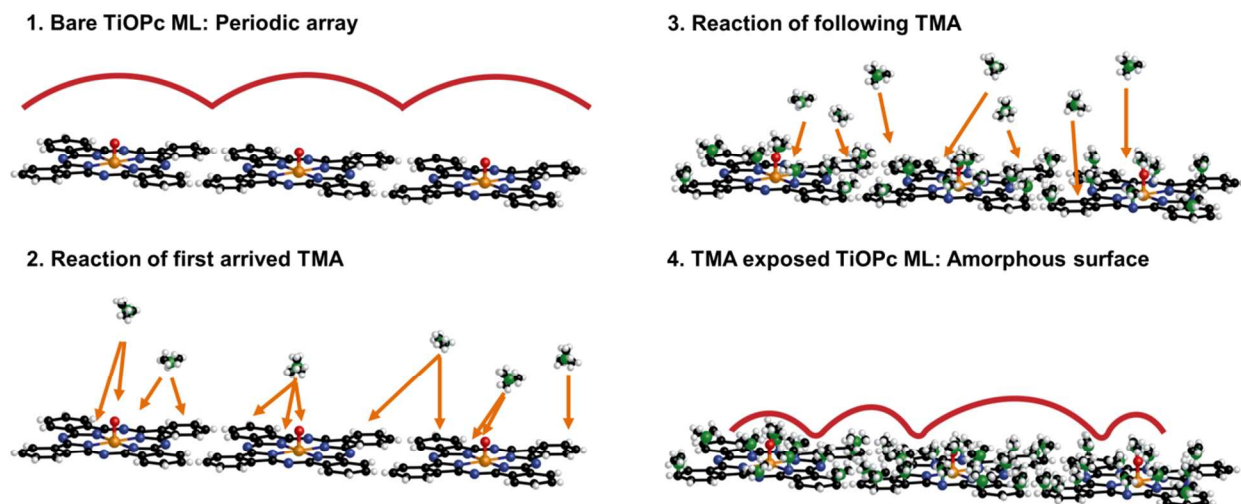


Figure S12. Schematic diagram for forming of TMA chemisorbates on TiOPc/HOPG. The forming TMA induced chemisorbates on TiOPc results in an amorphous spaced surface on TiOPc/HOPG. The expected STM topologies are drawn by red lines in the stage 1 and 4.

Although DFT calculations of DMA binding show that all of O, N and C sites have sufficient the binding energy to react with TMA at 393 K, some of carbon sites would not react with TMA during the first ALD pulse, because of the relatively lower binding energy of carbon sites compared to O and N with DMA. The stage 1 displays TiOPc monolayer forming a periodic array on HOPG and the expected STM topologies is displayed by the red line. In the stage 2 of Fig S12, since O and N have higher binding energy with DMA than C, it is hypothesized that the initial TMA adsorbates would react with O and N, while few TMA molecules would react with carbon sites. Afterwards, it is hypothesized that TMA would react with the carbon sites randomly, because all of carbon sites provide about 1.53 eV binding energy to the dissociation products (DMA). As shown in the DFT calculation in Fig. S11, coexistence of multiple DMA molecules on N (2.2~2.3 eV) can provide higher binding energy than single DMA on N (2.02 eV);, therefore, by it can be hypothesized that TMA is likely to react with carbon sites near the pre-reacted DMA, as shown in the stage 3 of Fig S12. By this process, the clusters of DMA chemisorbates form

independently on the spacing of TiOPc monolayer, consistent with inducing amorphous spaced DMA chemisorbates as shown expected STM topologies (red line) of the stage 4.

6. AFM images after ALD on bare HOPG, TiOPc/HOPG and TiOPc/graphene.

In this report, most STM experiments were performed on HOPG. Although graphene and graphite surfaces have different electronic properties, both graphene and graphite have inert surfaces because of the absence of dangling surface bonds in both graphene and graphite^{4, 21}. Therefore, STM results for TiOPc/HOPG can be assumed identical to experiments on TiOPc/graphene. Tapping-mode AFM was employed to characterize graphite and graphene surface after ALD deposition. Bare HOPG, TiOPc/HOPG and TiOPc/graphene/SiO₂/Si surface were exposed to 5 ALD cycles of 200 ms of TMA and 50 mS H₂O at 393 K. On HOPG surfaces where ALD was deposited, multiple pinholes of various sizes are observed with 0.75 ± 0.036 nm RMS (root mean square) roughness, as shown in Fig S13(a). Due to pinhole generation, the AlO_x layer is discontinuous, consistent with previous reports^{22, 23}. Employing a TiOPc seed layer induces a significant improvement in both HOPG and graphene surfaces dosed with ALD. As shown in Fig. S13(b) and (c), after 5 cycles of ALD on TiOPc/HOPG and TiOPc/graphene, the resulting layer is uniform, continuous and has a low-defect density, illustrating the impact of the TiOPc seed layer. The RMS surface roughness is subnanometer: 0.28 ± 0.028 nm for AlO_x/TiOPc/HOPG and 0.35 ± 0.038 nm for AlO_x/TiOPc/graphene. It is hypothesized that AlO_x/TiOPc/graphene/SiO₂/Si has slightly larger RMS roughness than AlO_x/TiOPc/HOPG because of the presence of the SiO₂/Si substrate, which is less uniform than HOPG. In summary, the post-ALD AFM images show that the TiOPc seed layer results in a uniform, high-quality deposition of AlO_x on both HOPG and graphene surfaces.

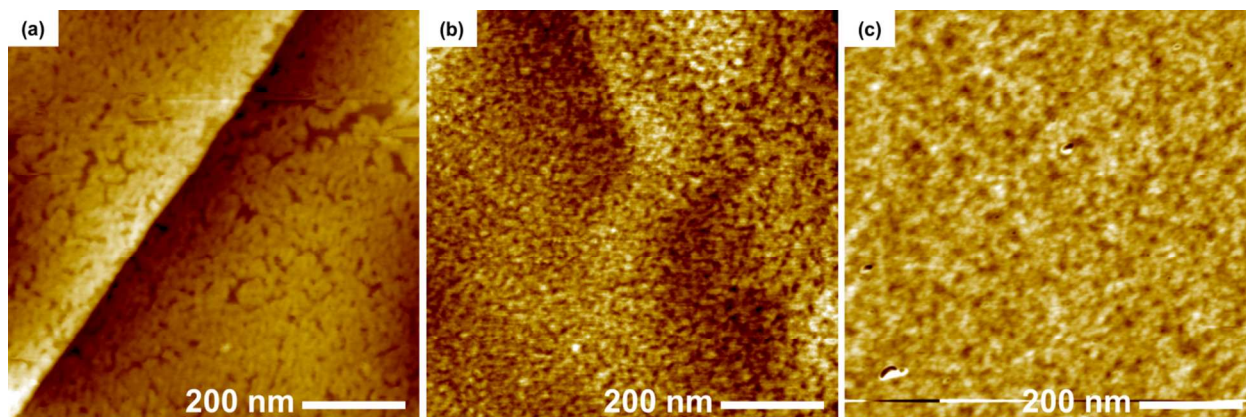


Figure S13. AFM images after 5 cycle ALD pulse. (a) ALD on HOPG, (b) ALD on TiOPC/HOPG, (c) ALD on TiOPc/Single layer graphene/SiO₂/Si. While ALD on the bare HOPG results in pinhole formation, ALD on the TiOPc/HOPG and TiOPc/graphene does not result in pinhole formation observable by AFM.

7. Observation charge trap states in AlO_x/TiOPc/HOPG by STS.

Figure S14 is an STS scan of 0.1 nm AlO_x/TiOPc/HOPG versus sample bias. The offset bias occurs at 1.5 V in the forward sweep (sweep range of -2.5 to 2.5 V), while the offset bias is observed in the reverse sweep is -0.6 V. These data are consistent with charge trapping in 0.1 nm AlO_x/TiOPc/HOPG, during the electron transfer between the tip and the sample through the AlO_x tunnel barrier.

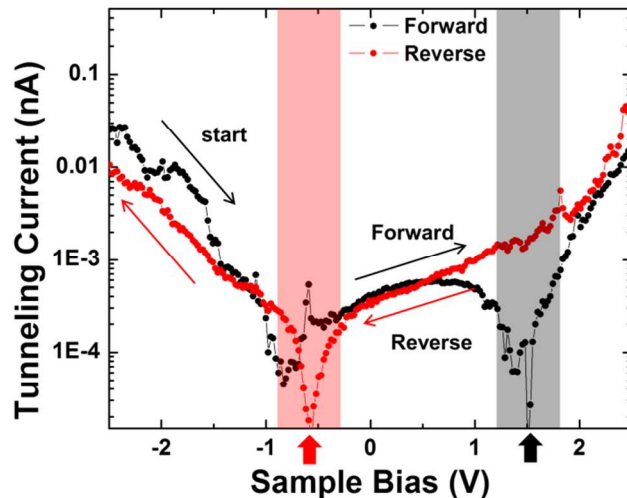


Figure S14. Scanning tunneling current versus sample bias on 0.1 nm $\text{AlO}_x/\text{TiOPc}/\text{HOPG}$. Positions of offset bias in negative and positive region are marked by red and black bars, respectively. (red and black arrows also are added at x axis.)

8. Capacitance-Voltage curves with expanded frequencies.

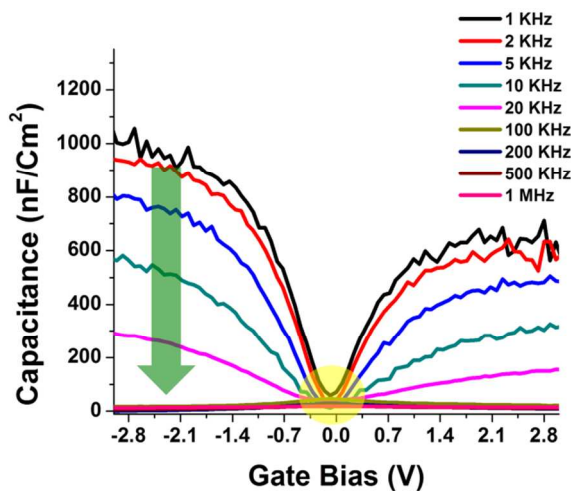


Figure S15. Capacitance-Voltage curves with variable frequencies (from 1KHz to 1MHz). As an increase of frequency from 1 KHz to 1MHz, the C_{max} is decreased significantly, while minimum capacitance values are nearly intact as shown in a yellow mark.

The capacitance-gate bias curves are plotted in Fig S15 with expanded frequency ranges. The C_{\max} is decreased significantly by increasing frequency (green arrow) consistent with series resistance: the V-shaped CV curve at low frequencies (1kHz~20kHz) is converted into inverse V-shape at high frequencies (100kHz~1MHz). It is noted that the minimum capacitance value is nearly constant and remain at 0 V as the frequency varied, indicating there is very low interface trap density. It can be hypothesized that there is high contact resistance between metal contact and graphene^{24, 25}. The other possible explanation is that since the maximum size of the grain boundaries of CVD graphene is only about 20 μm and TiOPc seedling layer could not been deposited well near these grain boundaries resulting defects, such as pinholes^{7, 8}. Although these pinholes were not observed in AFM images indicating very small sizes, they still can induce leakage in dielectrics.

9. MoS₂-ALD dielectric-TiOPc-graphene interlayer device.

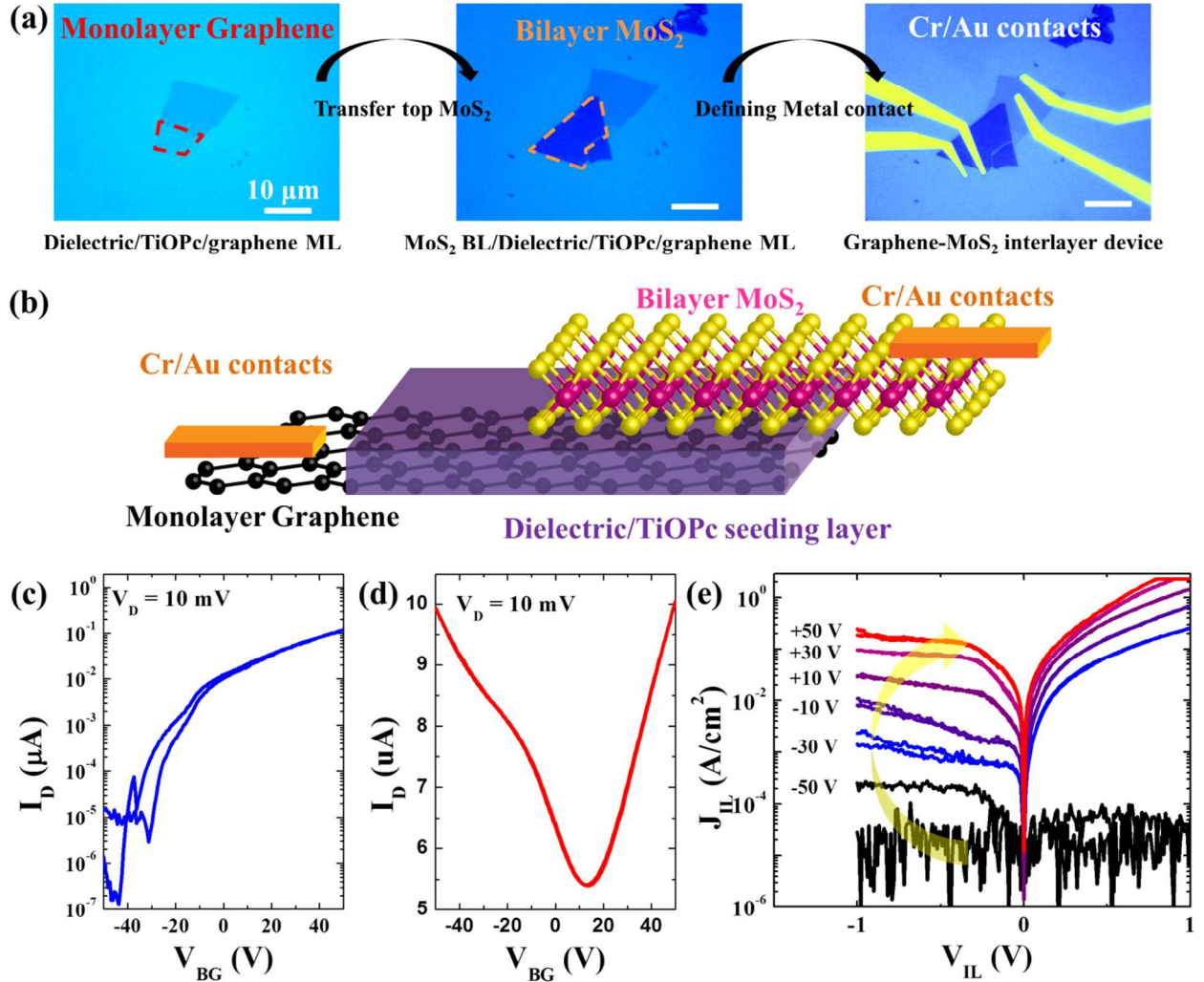


Figure S16. Fabrication and characteristics of MoS₂-ALD dielectric-TiOPc-graphene interlayer device. (a) Process flow of fabricating interlayer device. The aluminum oxide (50 cycles) was deposited onto TiOPc/graphene ML. Subsequently, a bilayer MoS₂ flake was transferred onto the AlO_x/TiOPc/graphene. Finally metal contacts were deposited by E-beam evaporation. (b) Schematic diagram of MoS₂-ALD dielectric-TiOPc-graphene interlayer device. (c) Drain current versus V_{BG} of the top MoS₂ BL channel. (d) Drain current versus V_{BG} of the bottom graphene ML channel. (e) Interlayer device tunneling current characteristics of the bottom graphene-top MoS₂ channels over deposited ALD dielectric/TiOPc.

The MoS₂-ALD dielectric-TiOPc-graphene interlayer device was fabricated to show the potential application for Tunneling FETs, employing the ALD dielectric as an interlayer dielectric. Figure S16(a) displays the process flow of fabricating the interlayer FET; a monolayer graphene was transferred onto the SiO₂/Si substrate, then TiOPc monolayer and ALD AlO_x were deposited sequentially. Afterwards, a bilayer of MoS₂ was transferred onto AlO_x/TiOPc/graphene/SiO₂/Si to form a heterostructure. Finally Cr/Au metal contacts were defined by using E-beam lithography and deposition. The final structure of interlayer device is displayed in Fig. S16(b).

The gating characteristic I_D versus V_{BG} of the top MoS₂ channel at constant $V_D = 10$ mV are shown in Fig. S16(c). The onset of drain current occurs at about $-30 \sim -40$ V_{BG}, indicating an n-type channel, and the ON/OFF ratio is obtained as about 10^5 . In figure S16(d), the drain current characteristics of bottom graphene channel versus V_{BG} are shown; the Dirac point is located at about $V_{BG} = +16$ V, indicating slightly p-type channel, and V shape of drain current density versus bias is displayed as function of V_{BG} from -50 V to +50 V. The interlayer tunneling current density (J_{IL}) versus the interlayer voltage (V_{IL}) measured at room temperature is shown in Fig. S16(e). At $V_{BG} = -50$ V, the interlayer current is at the noise level due to the MoS₂ being OFF. As V_{BG} is increased to -30 V, the MoS₂ accumulates electrons, while the graphene is still populated with holes. This causes an onset of tunneling current for positive V_{IL} , which increases exponentially with V_{IL} , and a low saturated J_{IL} for negative values of V_{IL} . This asymmetric dependence of J_{IL} on V_{IL} is characteristic of a diode formed between the n-type MoS₂, and p-type graphene. The ON/OFF ratio is found to be around 10^2 . Increasing V_{BG} from -30 V to +50 V causes an increase in both the ON and OFF currents, with the OFF current showing a large increases versus V_{BG} than the ON current. This gate-tunable heterojunction diode highlights the potential of the ALD dielectric towards building more complicated heterostructures devices.

Reference

1. Takami, T.; Clark, A.; Caldwell, R.; Mazur, U.; Hipps, K. W. *Langmuir* **2010**, 26, 12709-12715.
2. Kong, X. H.; Wang, M.; Lei, S. B.; Yang, Y. L.; Wang, C. *J Mater Chem* **2006**, 16, 4265-4269.
3. Matsui, T.; Kambara, H.; Niimi, Y.; Tagami, K.; Tsukada, M.; Fukuyama, H. *Phys Rev Lett* **2005**, 94, 226403.
4. Li, G. H.; Luican, A.; Andrei, E. Y. *Phys Rev Lett* **2009**, 102, 176804.
5. Feenstra, R. M. *Phys Rev B* **1994**, 50, 4561-4570.
6. Feenstra, R. M.; Lee, J. Y.; Kang, M. H.; Meyer, G.; Rieder, K. H. *Phys Rev B* **2006**, 73, 035310.
7. Li, X. S.; Cai, W. W.; An, J. H.; Kim, S.; Nah, J.; Yang, D. X.; Piner, R.; Velamakanni, A.; Jung, I.; Tutuc, E.; Banerjee, S. K.; Colombo, L.; Ruoff, R. S. *Science* **2009**, 324, 1312-1314.
8. Suk, J. W.; Kitt, A.; Magnuson, C. W.; Hao, Y. F.; Ahmed, S.; An, J. H.; Swan, A. K.; Goldberg, B. B.; Ruoff, R. S. *Acs Nano* **2011**, 5, 6916-6924.
9. Kresse, G.; Hafner, J. *Phys Rev B* **1993**, 47, 558-561.
10. Kresse, G.; Hafner, J. *Phys Rev B* **1994**, 49, 14251-14269.
11. Kresse, G.; Furthmuller, J. *Comp Mater Sci* **1996**, 6, 15-50.
12. Kresse, G.; Furthmuller, J. *Phys Rev B* **1996**, 54, 11169-11186.
13. Blochl, P. E. *Phys Rev B* **1994**, 50, 17953-17979.
14. Kresse, G.; Joubert, D. *Phys Rev B* **1999**, 59, 1758-1775.
15. Perdew, J. P.; Burke, K.; Ernzerhof, M. *Phys Rev Lett* **1996**, 77, 3865-3868.
16. Perdew, J. P.; Burke, K.; Ernzerhof, M. *Phys Rev Lett* **1997**, 78, 1396-1396.
17. Wu, X.; Vargas, M. C.; Nayak, S.; Lotrich, V.; Scoles, G. *J Chem Phys* **2001**, 115, 8748-8757.
18. Grimme, S. *J Comput Chem* **2006**, 27, 1787-1799.
19. Groner, M. D.; Fabreguette, F. H.; Elam, J. W.; George, S. M. *Chem Mater* **2004**, 16, 639-645.
20. Potts, S. E.; Profijt, H. B.; Roelofs, R.; Kessels, W. M. M. *Chem Vapor Depos* **2013**, 19, 125-133.

21. Terrones, M.; Botello-Mendez, A. R.; Campos-Delgado, J.; Lopez-Urias, F.; Vega-Cantu, Y. I.; Rodriguez-Macias, F. J.; Elias, A. L.; Munoz-Sandoval, E.; Cano-Marquez, A. G.; Charlier, J. C.; Terrones, H. *Nano Today* **2010**, *5*, 351-372.
22. Alaboson, J. M. P.; Wang, Q. H.; Emery, J. D.; Lipson, A. L.; Bedzyk, M. J.; Elam, J. W.; Pellin, M. J.; Hersam, M. C. *Acs Nano* **2011**, *5*, 5223-5232.
23. Jandhyala, S.; Mordi, G.; Lee, B.; Lee, G.; Floresca, C.; Cha, P. R.; Ahn, J.; Wallace, R. M.; Chabal, Y. J.; Kim, M. J.; Colombo, L.; Cho, K.; Kim, J. *Acs Nano* **2012**, *6*, 2722-2730.
24. Russo, S.; Craciun, M. F.; Yamamoto, M.; Morpurgo, A. F.; Tarucha, S. *Physica E* **2010**, *42*, 677-679.
25. Xia, F. N.; Perebeinos, V.; Lin, Y. M.; Wu, Y. Q.; Avouris, P. *Nat Nanotechnol* **2011**, *6*, 179-184.